

# JADES. Possible Population III signatures at $z=10.6$ in the halo of GN-z11

Roberto Maiolino<sup>1,2,3,\*</sup>, Hannah Übler<sup>1,2</sup>, Michele Perna<sup>4</sup>, Jan Scholtz<sup>1,2</sup>, Francesco D'Eugenio<sup>1,2</sup>, Callum Witten<sup>5,1</sup>, Nicolas Laporte<sup>1,2</sup>, Joris Witstok<sup>1,2</sup>, Stefano Carniani<sup>6</sup>, Sandro Tacchella<sup>1,2</sup>, William M. Baker<sup>1,2</sup>, Santiago Arribas<sup>4</sup>, Kimihiko Nakajima<sup>7</sup>, Daniel J. Eisenstein<sup>8</sup>, Andrew J. Bunker<sup>9</sup>, Stéphane Charlot<sup>10</sup>, Giovanni Cresci<sup>11</sup>, Mirko Curti<sup>12</sup>, Emma Curtis-Lake<sup>13</sup>, Anna de Graaff<sup>14</sup>, Eiichi Egami<sup>15</sup>, Zhiyuan Ji<sup>15</sup>, Benjamin D. Johnson<sup>8</sup>, Nimisha Kumari<sup>16</sup>, Tobias J. Looser<sup>1,2</sup>, Michael Maseda<sup>17</sup>, Brant Robertson<sup>18</sup>, Bruno Rodríguez Del Pino<sup>4</sup>, Lester Sandles<sup>1,2</sup>, Charlotte Simmonds<sup>1,2</sup>, Renske Smit<sup>19</sup>, Fengwu Sun<sup>15</sup>, Giacomo Venturi<sup>6</sup>, Christina C. Williams<sup>20</sup>, and Christopher N. A. Willmer<sup>15</sup>

(Affiliations can be found after the references)

## ABSTRACT

Finding the first generation of stars formed out of pristine gas in the early Universe, known as Population III (PopIII) stars, is one of the most important goals of modern astrophysics. Recent models suggest that PopIII stars may form in pockets of pristine gas in the halo of more evolved galaxies. Here we present NIRSpect-IFU and NIRSpect-MSA observations of the region around GN-z11, an exceptionally luminous galaxy at  $z = 10.6$ , which reveal a  $>5\sigma$  detection of a feature consistent with being HeII $\lambda$ 1640 emission at the redshift of GN-z11. The very high equivalent width of the putative HeII emission in this clump (170 Å), and the lack of metal lines, can be explained in terms of photoionisation by PopIII stars, while photoionisation by PopII stars is inconsistent with the data. It would also indicate that the putative PopIII stars likely have a top-heavy initial mass function (IMF), with an upper cutoff reaching at least 500  $M_{\odot}$ . The PopIII bolometric luminosity inferred from the HeII line would be  $\sim 2 \times 10^{10} L_{\odot}$ , which (with a top-heavy IMF) would imply a total stellar mass formed in the burst of  $\sim 6 \times 10^5 M_{\odot}$ . We find that photoionisation by the Active Galactic Nucleus (AGN) in GN-z11 cannot account for the HeII luminosity observed in the clump, but can potentially be responsible for additional HeII emission observed closer to GN-z11. We also consider the possibility of in-situ photoionisation by an accreting Direct Collapse Black Hole (DCBH) hosted by the HeII clump; we find that this scenario is less favoured, but it remains a possible alternative interpretation. We also report the detection of a Ly $\alpha$  halo stemming out of GN-z11 and extending out to  $\sim 2$  kpc, as well as resolved, funnel-shaped CIII] emission, likely tracing the ionisation cone of the AGN.

**Key words.** Stars: Population III - Galaxies: high-redshift - (Cosmology:) dark ages, reionization, first stars

## 1. Introduction

The formation of the first stars and galaxies marks a fundamental transitional phase in cosmic history, during which the Universe evolved from a relatively simple state into the highly structured system we observe today (Bromm & Larson 2004). Almost all baryonic matter formed after the Big Bang and the “dark ages” is composed of hydrogen and helium. Consequently, the very first stars to form must have condensed out of these elements, primarily as a result of cooling due to the small amounts of H<sub>2</sub> that could form at such early epochs (e.g. Kashlinsky & Rees 1983). These stars, called Population III (PopIII), are potentially very massive, up to several 100  $M_{\odot}$ , as a consequence of inefficient gas cooling and hence poor fragmentation of pre-stellar cores at these early epochs (e.g. Bromm et al. 1999, Abel et al. 2002, Tan & McKee 2004; Hirano et al. 2014; Susa et al. 2014). Indirect studies of Pop III stars via stellar archaeology confirm these predictions, suggesting that their masses extend up to 1000  $M_{\odot}$  with a characteristic mass  $> 1 M_{\odot}$  (Rossi et al. 2021; Pagnini et al. 2023). Such massive PopIII stars are expected to be very hot and leading to an energetic photoionising spectrum, capable of doubly ionising helium. Indeed, an expected signature of PopIII stars is prominent HeII nebular lines, with very large equivalent widths (EW(HeII $\lambda$ 1640)  $> 20$  Å), unaccompanied by metal

lines (Tumlinson & Shull 2000, Oh et al. 2001, Tumlinson et al. 2001, Schaerer 2003, Nakajima & Maiolino 2022). However, other models have also predicted that primordial gas might fragment more efficiently, resulting into the formation of cooler and less massive stars (e.g. Clark et al. 2011; Greif et al. 2011, 2012; Stacy et al. 2016)

While observations have found potential chemical fingerprints of the enrichment produced by the first generation of stars (Beers & Christlieb 2005; Frebel et al. 2007; Cooke et al. 2011; Hartwig et al. 2015, 2018; Salvadori et al. 2023; Saccardi et al. 2023; Klessen & Glover 2023), PopIII stars in early galaxies have eluded detection so far, with some claims not confirmed by subsequent studies (Sobral et al. 2015, Bowler et al. 2017, Harikane et al. 2018). However, the unprecedented sensitivity of JWST is pushing the frontier of observations to high redshift and very faint galaxies, discovering very low metallicity systems (Vanzella et al. 2023), indicating that the detection of PopIII stars may be within reach of this observatory (see also e.g. Zackrisson et al. 2011).

Further encouraging expectations about the detectability of PopIII stars have been obtained by recent cosmological simulations. Indeed, two main formation phases of PopIII stars have been proposed: firstly, PopIII stars could have formed in dark matter mini haloes at redshifts  $z \sim 10$ -30 (e.g. Tegmark et al. 1997; Bromm et al. 2009; Pallottini et al. 2014; Jeon et al. 2015,

\* rm665@cam.ac.uk

Vikaeus et al. 2022; Ventura et al. 2023; Trinca et al. 2023b). Secondly, PopIII stars could still have formed at later times, down to redshifts of about  $z \sim 3-6$ , in pristine/low-metallicity pockets of gas due to the highly inhomogeneous nature of metal enrichment in the Universe, as well as a consequence of re-accretion of pristine gas (e.g. Tornatore et al. 2007a; Johnson 2010; Liu & Bromm 2020, Sarmiento et al. 2018; Jaacks et al. 2019, Katz et al. 2022, Volonteri et al. 2023). In these cases, PopIII stars are expected to be found in the haloes of more massive galaxies, and their hard ionizing spectrum may be ionizing mildly enriched gas, resulting in weak emission of metal lines (Nakajima & Maiolino 2022, Katz et al. 2022, Jaacks et al. 2018).

Although in the latter scenario PopIII stars are expected to be present even at relatively low redshifts (possibly down to  $z \sim 3$ ; Cassata et al. 2013, Liu & Bromm 2020), the probability for a halo to host PopIII stars is higher at very high redshift (Trinca et al. 2023a). Within this context, GN-z11 is an exceptional galaxy at  $z=10.6$  which offers an optimal environment for searching PopIII stars. Identified initially by Bouwens et al. (2010); Oesch et al. (2016), GN-z11 is the most luminous galaxy at  $z > 10$  in all HST fields (including all CANDELS and Frontier Fields, Oesch et al. 2018). Recent JWST-NIRCam imaging from the JWST Advanced Deep Extragalactic Survey (JADES; D. Eisenstein, in prep.) revealed that GN-z11 is characterized by an unresolved central source, a more extended component (200 pc in radius) with Sérsic index  $n=1$ , and a more diffuse component extending for  $\sim 0.5''$  to the NE (the ‘haze’), which may not be associated with GN-z11 and could simply be a foreground system (Tacchella et al. 2023). Bunker et al. (2023) obtained low and medium resolution spectroscopy of GN-z11 with JWST-NIRSpec in the multi-object spectroscopy (MOS) mode using the micro-shutter assembly (MSA), revealing a spectrum with a wealth of nebular emission lines in various ionization stages, and also characterized by some unusual line ratios. Interestingly, the spectrum reveals  $\text{Ly}\alpha$  emission, extended along the slit for about  $0.4''$  ( $\sim 1.6$  kpc) towards the SW (the position angle of the shutter was  $19.9^\circ$ ). Additional NIRSpec MSA observations targeting GN-z11 have led to the identification of an active galactic nucleus (AGN) in GN-z11 (Maiolino et al. 2023), primarily through the detection of high ionization lines (NeIV), semi-forbidden lines tracing very high densities consistent with the Broad Line Regions (BLR) of AGN, and the detection of the  $\text{CII}^* \lambda 1335$  fluorescent emission, typically seen only in AGN. The spectrum of GN-z11 has also revealed the presence of a powerful outflow, traced by the redshifted ( $\sim 530 \text{ km s}^{-1}$ ) resonantly scattered emission of both  $\text{Ly}\alpha$  and  $\text{CIV} \lambda 1550$ , and blueshifted absorption of CIV ( $\sim 800 - 1000 \text{ km s}^{-1}$ ). The second NIRSpec MSA observation had a position angle nearly perpendicular to the first observation, and did not show obvious evidence for  $\text{Ly}\alpha$  extension on either side of GN-z11.

A more detailed analysis of the 2D spectrum of GN-z11 in the first observation revealed the tentative emission of a line located at  $\sim 0.5''$  to the NE of GN-z11, at a wavelength consistent with  $\text{HeII} \lambda 1640$  at the same redshift of GN-z11 (see Sect. 3.1). This intriguing finding prompted a DDT proposal to obtain NIRSpec-IFU spectroscopy of GN-z11 with both the G140M (3.3 h) and G235M (10.6 h) gratings. The IFU datasets deliver superior spatial information relative to the MSA (although the sensitivity is lower than the MSA, because the IFU has about 50% lower throughput).

In this paper we report a preliminary analysis of the new NIRSpec IFS data of GN-z11, which confirm the  $\text{HeII} \lambda 1640$  de-

tection at  $z=10.6$ , as well as additional interesting features associated with the  $\text{Ly}\alpha$  and  $\text{CIII}]$  morphology.

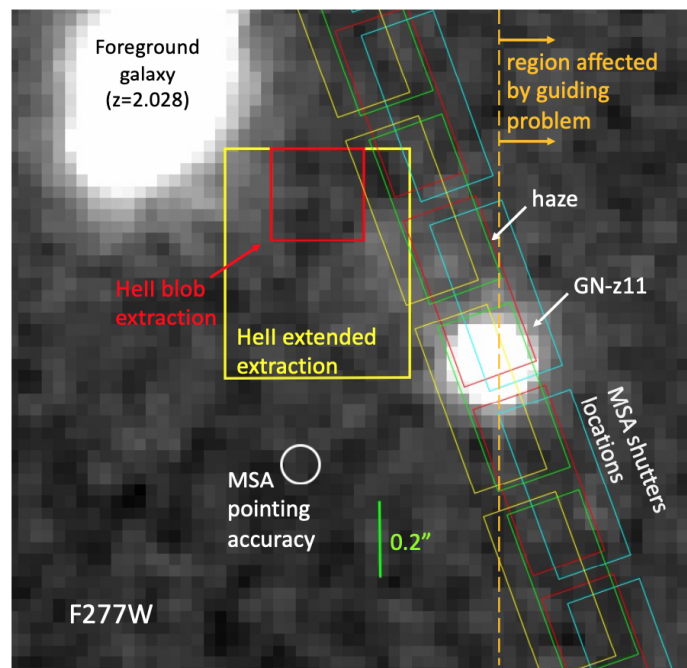


Fig. 1: F277W NIRCam image of the central  $\sim 1.7''$  around GN-z11 illustrating the location of the MSA shutters during the first NIRSpec-MOS observations in February 2023 (tilted boxes, with boxes of the same color being associated with the same configuration), extraction region of the HeII clump (red square) and of the HeII extended emission (yellow box). The white circle indicates the absolute uncertainty of the MSA target acquisition (hence the shutters’ footprints are uncertain by this amount). North is up and East is to the left. The vertical dashed orange line marks the boundary beyond which fewer dithers from the NIRSpec IFU observations are available because of the guiding problem reported in Sect. 2. Note that the full IFU field of view is larger than shown here ( $> 3'' \times 3''$  taking into account the dithers).

Throughout this work, we use the AB magnitude system and assume a Planck flat  $\Lambda$ CDM cosmology with  $\Omega_m = 0.315$  and  $H_0 = 67.4 \text{ km/s/Mpc}$  (Planck Collaboration et al. 2020). With this cosmology  $1''$  corresponds to a transverse distance of 4.08 proper kpc at  $z = 10.6$ .

## 2. Observations, data processing and data analysis

GN-z11 was observed with NIRSpec IFU (Jakobsen et al. 2022; Böker et al. 2022) on May 22<sup>nd</sup> – 23<sup>rd</sup> 2023 under the DDT program 4426 (PI: Roberto Maiolino). The observational setup utilised a medium cycling pattern of 10 dithers for a total integration time on source of 10.6 h with the medium-resolution grating/filter pair G235M/F170LP, and 3.3 h with the medium-resolution grating/filter pair G140M/F100LP. These configurations cover the spectral ranges of 0.97–1.89 and 1.66–3.17  $\mu\text{m}$ , with a nominal spectral resolution of  $R \sim 1000$ . The detector was set with the improved reference sampling and subtraction pattern (IRS<sup>2</sup>), which reduces significantly the read out noise with respect to the conventional method (Rauscher et al. 2012). We also checked that no bright foreground sources were at the

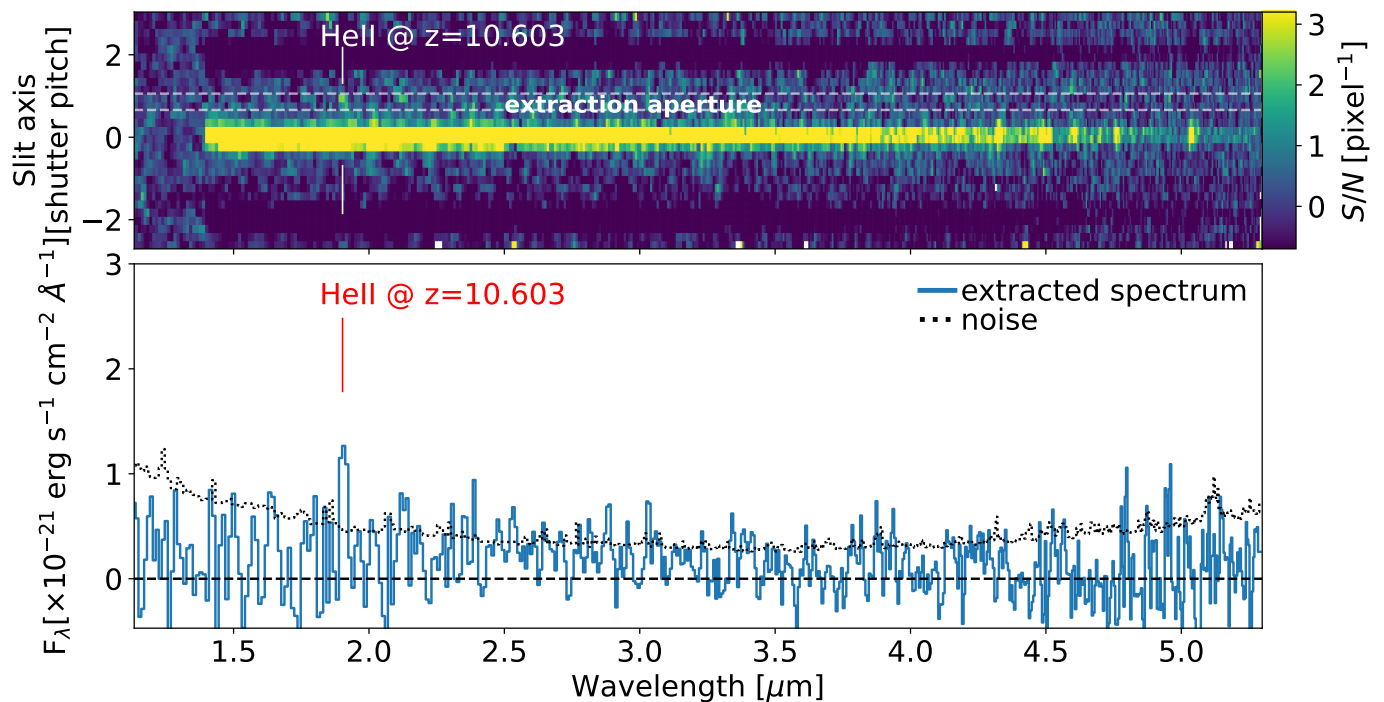


Fig. 2: Top panel: Signal-to-noise 2D prism spectrum of GN-z11 from the February 2023 MSA observation, reprocessed to use only the exposures in which GN-z11 is in the upper and lower shutters (hence discarding the exposure with GN-z11 in the central shutter), so to avoid self-subtraction of extended signal. Bottom panel: 1D spectrum extracted from the region delimited by the two dashed horizontal lines, at about  $0.45''$  from GN-z11 in the NE direction, illustrating the tentative detection ( $3.7 \sigma$  integrated) of a feature at  $1.903 \mu\text{m}$ . The red vertical line indicates the location of HeII $\lambda$ 1640 expected at the redshift of GN-z11,  $z=10.603$  (which is undistinguishable from the redshift of 10.600 inferred for the grating spectrum).

location of the MSA quadrants where they could significantly contaminate the IFS spectra.

Although JWST has an excellent pointing accuracy (i.e.  $0.1''$ ,  $1 \sigma$  radial<sup>1</sup> Rigby et al. 2023), and the telescope was commanded to the location of GN-z11 provided by the NIRCcam and HST imaging and GAIA-referenced astrometry, the observations were affected by a guiding problem of the observatory, because the guide star turned out to be a binary (report from the FGS team); this introduced a large off-set of about  $1.4''$  towards the SE. This offset located GN-z11 close to the edge of the IFU FoV. This restricted the zone around GN-z11 that could be explored, lowering the S/N of regions which were covered by fewer dither positions, or excluding completely some regions from the FoV. More specifically, out of 10 dither positions, GN-z11 itself was located right at the edge of the FoV in three of them, and in another four of them GN-z11 is so close to the edge that the SW extension of the Ly $\alpha$  was mostly outside the FoV. Although in this paper we attempt an analysis of the SW extension based on the incomplete data, this will need to be validated by planned future observations that will repeat the dithers that were more severely affected (within the context of the same program 4426). As a consequence, the main focus of this paper is on the extended emission towards the NE.

Because of the guiding problem, the world coordinates given by the pipeline in the header of the final IFU cube are off by about  $1.4''$ . Therefore, we corrected the world coordinates by realigning the cube to the NIRCcam image, by collapsing the cube

in the same band as in the NIRCcam filter (although the centroid of the continuum does not change with wavelength).

Raw data files were downloaded from the MAST archive and subsequently processed with the JWST Science Calibration pipeline<sup>2</sup> version 1.8.2 under CRDS context `jwst_1068.pmap`. We made several modifications to the default reduction steps to increase data quality, which are described in detail by Perna et al. (2023) and which we briefly summarize here. The default pipeline is occasionally subject to over-subtraction of elongated cosmic ray artefacts, through the default circular correction applied to ‘snowball-like’ cosmic ray hits. To avoid this problem, we patched the pipeline to fit ellipses to all flagged regions consisting of five or more adjacent pixels; regions with best-fit ellipses having axial ratios smaller than 0.1 are removed from the list of ‘snowball-like’ cosmic rays. Count-rate frames were corrected for  $1/f$  noise through a polynomial fit. Outliers were flagged on the individual 2D exposures, using an edge-detection algorithm similar to LACOSMIC (van Dokkum 2001). We calculate the derivative of the count-rate maps along the x-axis of the detector (on the scale of a few pixels, the x-axis is a good approximation for the dispersion direction). The derivative was normalised by the local flux (or by 3 times the rms noise, whichever was highest), and we rejected the 95<sup>th</sup> percentile of the resulting distribution – the percentiles are calculated over the entire detector area (see F. D’Eugenio et al. 2023 for details). In addition, we made the following corrections to the `*cal.fits` files after Stage 2: we mask pixels at the edge of the slices (two pixels wide) to conservatively exclude pixels with unreliable flat corrections. We also mask regions that are affected through leak-

<sup>1</sup> <https://jwst-docs.stsci.edu/jwst-observatory-characteristics/jwst-pointing-performance>

<sup>2</sup> <https://jwst-pipeline.readthedocs.io/en/stable/jwst/introduction.html>

age from failed open MSA shutters. Note that the data quality flag ‘MSA\_FAILED\_OPEN’ fails to account for all failed open MSA shutters. At the same time, several regions marked as being affected by failed open shutters do not show any impact from leakage, and we include those regions to increase  $S/N$  in the final combined cube. Finally, we mask regions that are affected by persistence in all dither frames, e.g. from cosmic rays. The final cubes were combined using the ‘drizzle’ method with pixel scales of  $0.06''$  and  $0.10''$ , for which we used an official patch to correct a known bug<sup>3</sup>.

We also re-analyse the NIRSpec MOS observations of GN-z11 obtained in February 2023 within the JADES survey, but with focus on the 2D extraction along the shutters. These observations were described in Bunker et al. (2023). Here we only remind that those observations were obtained with three configurations of the MSA (Jakobsen et al. 2022; Ferruit et al. 2022; Böker et al. 2023), each with 3-shutters nodding. The low-resolution prism and the three medium-resolution gratings were used, for a total observing time of 6.9 hours with the prism and 3.45 hours with each of the gratings. In the following, to explore the 2D information we use only the prism, as the gratings exposures are shallower. The processing of the MSA data is also described in Bunker et al. (2023), here we only recall that we have used the pipeline developed by the ESA NIRSpec Science Operations Team and the NIRSpec GTO Team. We also recall that the spatial pixel size in the MSA 2D spectra is  $0.1''$  and that each shutter is  $0.2''$  wide. The standard background subtraction method does not allow to explore extended emission along the shutters. Indeed, the nodding technique moves the target by one shutter position, i.e. by  $0.''53$  along the shutters direction. When reciprocally subtracting two exposures in which the source is located in adjacent shutters, this results into a deep negative trace of the subtracted source spectrum at  $\pm 0.5''$  from the (positive) spectrum of the source, wide at least as much as the PSF ( $\sim 0.1''$ ) or more, depending on the source size. This makes the 2D spectrum unusable to explore any extended emission beyond  $\sim 0.2''$  from the source. Therefore, in order to explore the 2D information along the shutter and to avoid self-subtraction of the extended emission, in this paper we use a different background subtraction process relative to standard process adopted in Bunker et al. (2023). Specifically, we do not use the exposure with the source in the central shutter, and use only the exposures in which the source is in the upper and lower shutters (i.e. the most distant ones) to perform mutual background subtraction. This ensures that the subtracted, negative traces of the GN-z11 spectrum, are located at  $\sim 1''$  from the (positive) spectrum, and enables the study of spectral features along the shutter up to about  $0.6''$  from the source. This method obviously slightly reduces the sensitivity of the data, as we use only 2/3 of the data and also the noise in the background is increased by a factor of  $\sqrt{2}$ , but is far superior relative to the standard method in exploring extended emission.

The tilted boxes in Fig.1 show the footprint of the shutters in the four MSA configurations of the MOS observation in February 2023, overlaid on the F277W image of GN-z11 (Tacchella et al. 2023). The green circle indicates the target acquisition uncertainty of the MSA, meaning that the footprints indicated in the figure may actually be displaced in any direction by that amount. The dashed vertical orange line indicates the region beyond which fewer exposures from the NIRSpec IFU DDT programme are available (and at the edge of the field of view) because of the telescope guiding problem discussed above.

When extracting spectra and emission line maps, we remove background and continuum emission with the following procedure. We extract the background from an area of the IFU free from artefacts and by sigma-clipping outliers. The resulting spectrum is smoothed with a rolling median of 25 spectral pixels. This background is normalized to the continuum in the vicinity of the spectral feature and subtracted. Since the background has some residual structure across the IFU field of view, also because of the possible continuum contribution from individual sources (especially in the case of GN-z11), we further optimize the continuum subtraction by linearly interpolating the continuum within a range of a few  $0.01 \mu\text{m}$  around the line of interest. In the case of the  $\text{Ly}\alpha$  the latter step may be more problematic on GN-z11, as the galaxy continuum is asymmetric relative to  $\text{Ly}\alpha$  due to IGM absorption (which also affects the continuum redwards of the  $\text{Ly}\alpha$  because of the damping wing); however, we are primarily interested in the extended emission, where the galaxy continuum is not detected. We have further explored the subtraction of the continuum around  $\text{Ly}\alpha$  by fitting the continuum only on the red side of the line, and the result does not change, except for a slight increase in the noise on the extended component, as expected from the poorer sampling of the background.

### 3. Results

#### 3.1. HeII detection in the halo of GN-z11

We start by illustrating the tentative detection of HeII $\lambda 1640$  in the 2D spectrum along the shutters in the NIRSpec MSA observation of February 2023 where we show the  $S/N$  2D spectrum of GN-z11 in the top panel of Fig. 2. As already discussed, this was reprocessed to use only the exposures in which GN-z11 is in the upper and lower shutters (hence discarding the exposure with GN-z11 in the central shutter), to minimize self-subtraction of extended emission. The 2D spectrum shows a tentative signal at  $1.905 \mu\text{m}$ , which is the expected location of HeII $\lambda 1640$  at the redshift of GN-z11 ( $z=10.603$ ), peaking at about  $0.5''$  from GN-z11. The bottom panel shows the spectrum extracted from the region of the 2D spectrum delimited by the two horizontal dashed lines in the upper panel. The black dotted line indicates the noise level per spectral pixel. The extracted spectrum confirms the emission feature at  $1.905 \mu\text{m}$ . The integrated significance of the feature is  $3.7\sigma$ , as reported in Table 2. We note that this feature is totally impossible to detect with the standard background subtraction procedure adopted in Bunker et al. (2023), as in that case the deep negative trace of the GN-z11 subtracted spectrum falls exactly at this location: this is the first negative trace, next to the (positive) spectrum of GN-z11, in the top panel of Fig.1 of Bunker et al. (2023); with our method we avoid the negative traces nearest to the GN-z11 spectrum (i.e. those at  $\pm 0.5''$  from the spectrum of GN-z11 in the 2D spectrum of Bunker et al. (2023)). We also note that the absolute flux and spatial centroid of the feature are affected by some additional uncertainty associated with the 2D extraction. Specifically, the feature is at the edge of the region beyond which self-subtraction can still happen even by adopting our 2-shutters methodology; this can result into both flux uncertainty and the centroid being artificially shifted towards GN-z11. Secondly, in some exposure the feature falls next or beneath the shutter bar (see Fig. 1), this can also affect the flux and centroid. Finally, the aperture losses applied to the spectrum are based on the point-like assumption and by using the location of GN-z11; hence if the HeII emission is slightly extended this may result in additional flux uncertainties.

<sup>3</sup> <https://github.com/spacetelescope/jwst/pull/7306>

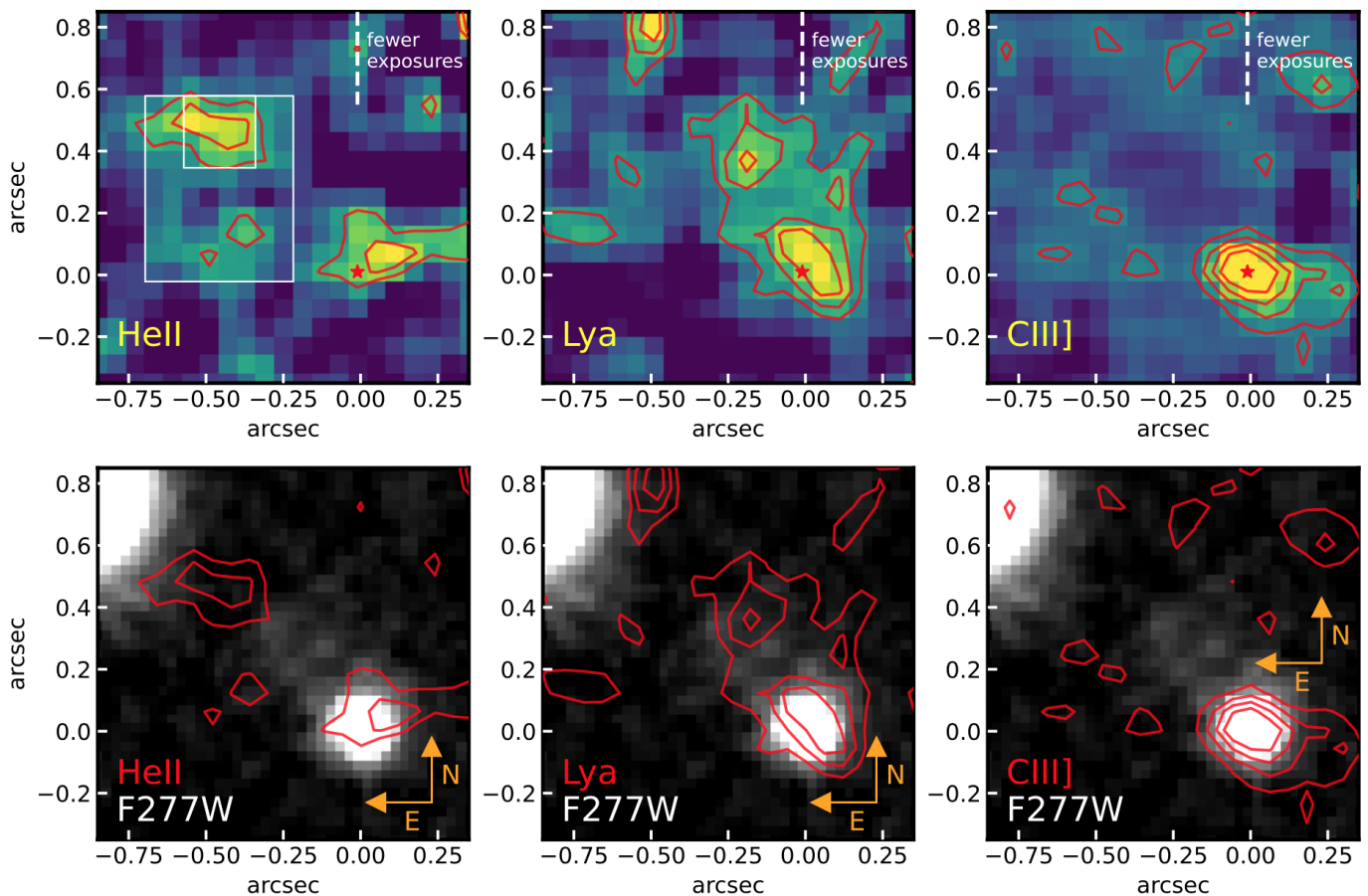


Fig. 3: Top panels: Maps of the HeII $\lambda$ 1640, Ly $\alpha$ , and CIII] $\lambda$ 1909 lines (see text for details). The red star marks the position of the continuum of GN-z11. Contours are at 2, 3 and 4  $\sigma$  for the HeII and Ly $\alpha$  maps, and at 2, 4, 6 and 8  $\sigma$  for the CIII] map (the rms is estimated from the statistics in the IFU field of view, outside this region). Note that most of these spaxels are independent, hence the significance of the integrated emission of each feature is significantly higher. The two white boxes indicate the extraction apertures of the two spectra shown in Fig. 4 and marked in red and yellow in Fig. 1. The vertical dashed segment indicates the region beyond which there are fewer exposures because of the guiding problem discussed in Sect. 2. Bottom panels: overlay of the contours from the emission line maps onto the F277W NIRCmap from Tacchella et al. (2023).

Fig. 3 shows the maps at the expected wavelengths of HeII, Ly $\alpha$  and CIII] obtained from the NIRSpect-IFU observation. Specifically, HeII and CIII] are centred at the expected wavelength of the two lines at the redshift of GN-z11,  $z=10.603$ , with a width of  $470 \text{ km s}^{-1}$  for HeII and  $780 \text{ km s}^{-1}$  for CIII] (as the latter is a doublet hence slightly broader, although still unresolved at our resolution). The Ly $\alpha$  map has been centred on the Ly $\alpha$  offset observed in GN-z11 ( $-550 \text{ km s}^{-1}$ ) with a width of  $500 \text{ km s}^{-1}$ . The maps are also slightly smoothed with a Gaussian Kernel with a width of 1.5 pixels ( $0.09''$ ).

Note that, since these features are extended, the significance of the integrated emission of the individual clumps is higher than that given by the contours.

The HeII map shows a plume extending for about  $0.25''$  towards the West of GN-z11. This is the area with fewer exposures (due to the guiding problem), so it should be treated with great care. Yet, if confirmed, such HeII plume would extend well beyond the size of the galaxy identified by Tacchella et al. (2023) and may be tracing gas photoionized by the AGN. The weak CIII] (and no CIV emission seen either at this location), would indicate that this is very low metallicity gas photoionized by the AGN.

The most intriguing feature is the clump located at about  $0.6''$  ( $2.4 \text{ kpc}$ ) to the NE. This is very close to the location of

the emission serendipitously found along the shutter of the MSA prism observation (Fig. 2), especially taking also into account the MSA target acquisition uncertainty and the fact that the MSA observation still suffers signal self-subtraction at locations farther than  $0.5''$  from GN-z11. We have extracted the spectrum from this region, by taking a  $0.24'' \times 0.24''$  square aperture (red box in Fig. 1, ‘HeII blob extraction’, smaller white box in Fig. 4 and Tab. 1). The resulting spectrum is shown in the top-left panel of Fig. 4, showing the detection of a line at  $\lambda_{\text{obs}} = 1.902 \mu\text{m}$ , whose integrated significance is  $5.5 \sigma$  (Table 2). This corresponds to the wavelength of HeII $\lambda$ 1640 at a redshift of 10.600, fully consistent with the redshift of GN-z11.

It is unlikely that this feature is H $\alpha$  or [OIII] $\lambda$ 5007 of a lower redshift interloper, specifically at  $z=1.90$  or  $z=2.80$ , as other bright lines expected at these redshifts are not seen. The ‘haze’ identified in imaging by Tacchella et al. (2023) is probably a lower redshift interloper, but is offset (closer to GN-z11) relative to the putative HeII clump; we indeed identify an emission line at  $2.330 \mu\text{m}$  peaking on the ‘haze’ that we tentatively identify as [OIII] at  $z=3.65$  (see Appendix B for details), consistent with the photometric redshift inferred by Tacchella et al. (2023). The foreground galaxy at  $z=2.28$  to the NW of the clump does not have any line emission at this wavelength (see spectrum in Appendix B), and any weak emission feature potentially associated

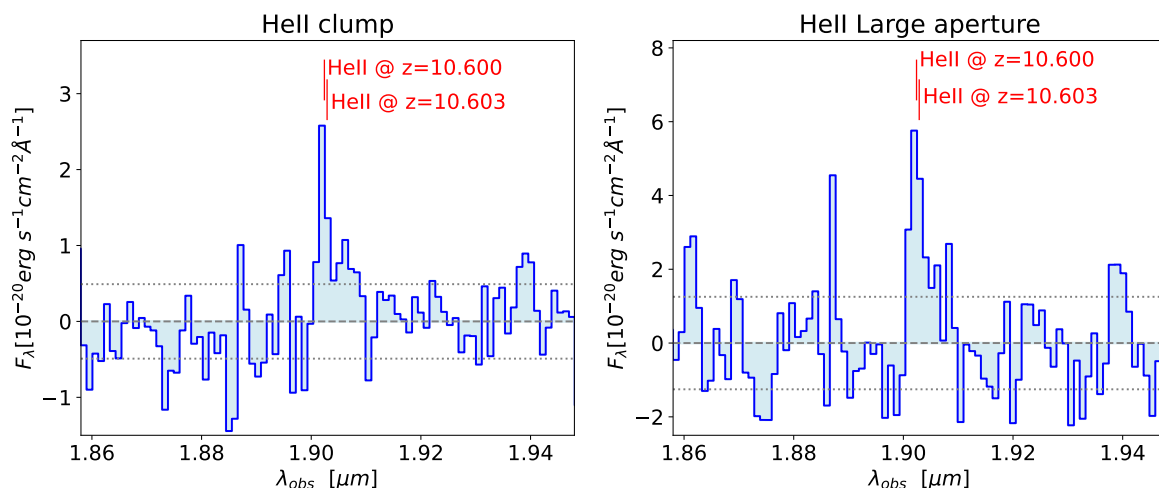


Fig. 4: Spectra extracted from the apertures indicated in Fig. 1, zoomed around the expected wavelength of HeII at the redshift of GN-z11. Specifically, the left panel shows the spectrum extracted from the aperture centered on the ‘HeII clump’ (red box in Fig. 1 and smaller white box in Fig. 3); the right panel shows the spectrum extracted from the larger aperture encompassing the extended HeII emission in the NE quadrant of GN-z11 (yellow box in Fig. 1 and larger white box in Fig. 3). The vertical red bars indicate the expected wavelength of HeII at the redshift of GN-z11,  $z=10.603$ , and the redshift corresponding to the centroid of the line in the HeII clump,  $z=10.600$ . The dotted lines indicate the noise per spectral pixel in each spectrum inferred from the rms directly measured in the spectrum around the HeII line.

with that galaxy would also show must stronger H $\alpha$  associated with it, as well as many other stronger emission lines.

We have also explored whether some Ly $\alpha$  emission is leaking out of the IGM absorption at this location. We found a tentative detection of Ly $\alpha$ , but which requires additional data for confirmation, so we do not discuss this any further.

It is difficult to compare the fluxes of the putative HeII seen in IFU clump and the detection in the MSA. In terms of wavelength they are fully consistent. In terms of flux it is more difficult. At face value, the fluxes reported in Tab. 2 give a flux in the MSA lower (with large error), as expected by the fact that the MSA shutter only picks part of the HeII clump. However, because of the uncertainty on the exact location of the MSA shutter (see Sect. 2 and white circle in Fig. 1) it is not known what is the actual fraction of the putative HeII clump that entered the shutters. Moreover, the absolute flux calibration plaguing the MSA, as discussed above, introduce additional uncertainties that prevent a proper comparison. Finally, we note that the MSA-Prism observation is more sensitive than the IFU observation (as discussed in Sect. 1) hence it may be detecting additional HeII emission outside the clump, not seen in the IFU cube.

In addition to the clump at  $\sim 0.6''$  to the NE from GN-z11, the HeII emission appears to have an additional, more extended emission, as seen in the map (Fig. 3 top-left), mostly distributed the NE quadrant of GN-z11, possibly with a fainter, less significant clump, about  $0.3''$  south of the HeII primary clump and about  $0.4''$  east of GN-z11. We have extracted the spectrum from this larger area by using the large aperture marked with the yellow box in Fig. 1. The resulting spectrum at the wavelength of HeII at  $z=10.600$  is shown in the right panel of Fig. 4. In this case the putative HeII emission is detected at  $6.1\sigma$  and with a total flux that is about two times higher than in the clump. We note that the putative HeII emission detected in this larger aperture is certainly not polluted by HeII emission in GN-z11. To begin with, the HeII emission of GN-z11 is very faint (Maiolino et al. 2023; Bunker et al. 2023); contamination by GN-z11 would imply that all other strong lines seen in GN-z11 would be detected, and much brighter than HeII. Secondly, in Appendix C we also

extract a spectrum by modifying this large aperture so to remove the region closer than  $0.3''$  (more than six times the PSF radius at this wavelength) from GN-z11, and the detection remains unchanged (Fig. C.1), therefore confirming that the weak HeII emission from GN-z11 does not contribute at all to the spectrum extracted in this region.

### 3.2. Ly $\alpha$ halo and morphology

Although not the focus of this paper, in middle panel of Fig. 3 we also show the map of the Ly $\alpha$  emission. Here we simply collapse the background/continuum-subtracted channels around the redshifted peak observed in GN-z11 (a more in depth analysis of the full Ly $\alpha$  profile will be presented in a forthcoming paper). The Ly $\alpha$  emission is clearly extended, partly in the Western direction (towards the same region as the HeII plume next to GN-z11), but mostly towards the SW, as expected from the MOS data when taken along this orientation (Bunker et al. 2023). The extension towards the SW is very sharp and could potentially trace an accreting filament. However, as discussed in the next Sect., the fact that we also see lop-sided CIII] emission in this direction favors the interpretation that the emission in the SW stems from gas illuminated in the ionization cone of the AGN in GN-z11. We however warn that this region falls in the area with less coverage because of the telescope guiding problem discussed in Sect. 2, so the emission in this region could potentially extend farther to the SW. A proper investigation requires additional data that will be obtained in the repeated observations.

At a low surface brightness level Ly $\alpha$  extends smoothly and over a larger area also towards the North, with a peak at about  $0.4''$  to the NE of GN-z11. The nature of the extended Ly $\alpha$  emission will be discussed more extensively in a dedicated paper.

### 3.3. CIII] extension and the ionization cone

The CIII]1909 doublet is one of the brightest metal lines observed in the spectrum of GN-z11, and is the only one that

is clearly resolved in the IFU observations. Its continuum-subtracted map is shown in the right panel of Fig. 3. The CIII] emission is clearly elongated in the NE-SW direction, and most prominently extended towards the SW with a funnel-shaped geometry (note that the elongation is not an artefact of the data processing, as demonstrated in the Appendix where we extract the continuum map around the same wavelength). The most plausible interpretation is that this emission is tracing the ionisation cone of the AGN in GN-z11. Although no CIV is clearly detected in this region (which however might be self-absorbed; Maiolino et al. 2023), the emission line properties are fully consistent with an AGN photoionisation scenario with low ionisation parameter, likely due to the distance from the AGN (Nakajima & Maiolino 2022). Once again, since this extended emission falls in the region where the exposure time is smaller because of the telescope guiding problem discussed above, the investigation of this extended emission will require the additional data that will be obtained in the repeated observations.

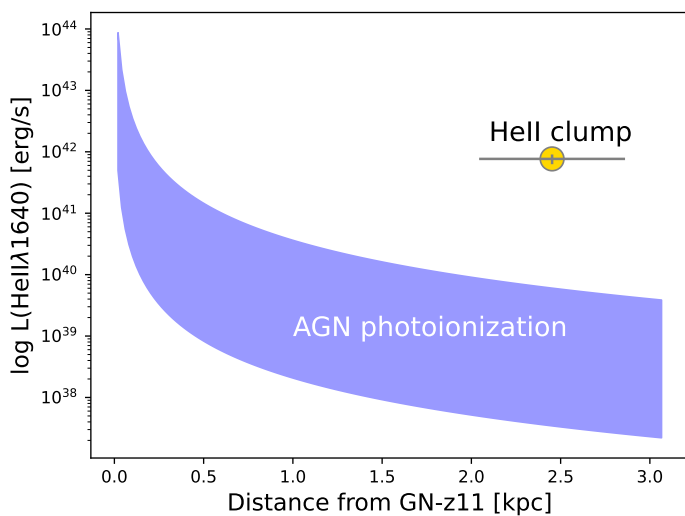


Fig. 5: Observed HeII $\lambda$ 1640 luminosity of the ‘HeII clump’ and its projected distance from GN-z11, compared to the expected HeII luminosity as a function of distance from GN-z11, in case of AGN photoionization. In this calculation, we use the upper limit for the size of the HeII clump and assume a broad range of AGN ionising shapes powering the photo-ionisation. Further conservative assumptions are that the ‘HeII clump’ is not made of unresolved clumps and that the projected distance is the actual separation. Clearly, the HeII luminosity observed in the ‘HeII clump’ is completely inconsistent with being photoionized by the AGN in GN-z11.

#### 4. The case for pristine gas and Population III

As discussed in Sect. 3.1, the most likely identification of the emission line observed at  $1.902 \mu\text{m}$  in the halo of GN-z11 is HeII $\lambda$ 1640 emission at  $z=10.600$ . In the vicinity of GN-z11, specifically the Western plume and some of the extended emission towards the NE quadrant, the HeII emission may likely trace gas photoionized by the AGN in GN-z11. The fact that no or little emission from metal lines (in particular CIV, CIII] and OIII]) is detected in these regions suggests that such circumgalactic gas has low metallicity. However, it is also possible that the low intensity of all metal lines is a consequence of low ionisation parameter (Feltre et al. 2016; Nakajima & Maiolino 2022). Yet,

empirically, when extended HeII emission is observed in other haloes surrounding AGN at lower redshift, this is always accompanied by even brighter CIV emission and possibly CIII] emission (Guo et al. 2020; Fossati et al. 2021). Therefore, the finding of extended HeII emission around an AGN at  $z>10$  not accompanied by CIV emission suggests that this is primarily due to much lower gas metallicity in the halo.

However, although the gas closer to GN-z11 may be photoionized by the AGN, the HeII emission seen in the NE clump at  $\sim 0.6''$  (2.4 kpc) from GN-z11 cannot be explained in terms of photoionisation by the AGN, simply based on ionising photons budget arguments. Indeed, HeII $\lambda$ 1640 is a simple recombination line, which therefore essentially is a counter of photons more energetic than 54 eV of the impinging radiation. As a consequence, knowing the luminosity of the AGN (Maiolino et al. 2023), as well as the distance and size of the cloud, one can estimate the number of HeI ionising photons reaching the cloud and the resulting HeII luminosity. We have assumed a broad range of AGN ionising spectra (Nakajima & Maiolino 2022) and that the observed, projected distance gives the actual distance of the clump to GN-z11. This obviously is a conservative assumption as the actual distance is larger and resulting into a lower flux of ionising photons. We also assume that, within the clump, the covering factor of the absorbing gas is unity, i.e. that the gas in the cloud is not ‘clumpy’, hence all radiation reaching it is fully absorbed. The result of this calculation is shown in Fig. 5 where the blue shaded area shows the expected HeII luminosity as a function of distance from GN-z11, assuming photoionisation by the AGN in GN-z11 and by adopting *all* AGN ionising continuum shapes considered in Nakajima & Maiolino (2022). We have also assumed isotropic emission, which is another conservative assumption given that the AGN in GN-z11 is type 1. The luminosity observed in the HeII clump ( $L(\text{HeII}) = 7.7 \times 10^{41}$  erg/s, based on the flux reported in Table 2) is shown with the golden symbol, which is clearly inconsistent with AGN photoionisation by about two orders of magnitude. Note that we have assumed stable emission, but it is very unlikely that the luminosity of the AGN can change by two orders of magnitude, even because the variability observed so far is constrained to the level of 10% (Maiolino et al. 2023).

The HeII emission in the clump must therefore result from *in-situ* photoionisation. In Fig. 6 we explore the source of ionising photons and gas metallicity by using diagnostic diagrams in which the equivalent width of the HeII line is compared with various line ratios, specifically: HeII/H $\gamma$ , CIV $\lambda$ 1550/HeII, CIII] $\lambda$ 1909/HeII, OIII] $\lambda$ 1665/HeII. We compared these quantities with the photoionisation models presented in Nakajima & Maiolino (2022). Specifically, the red stars illustrate the case of photoionisation by PopII stars (through metal poor models from the BPASS libraries), with a broad range of ionisation parameters and densities and with (absolute) metallicities ranging from  $10^{-5}$  to  $10^{-3}$ . In these models the gas and stars are assumed to have the same metallicity. The blue symbols show the models for PopIII ionising continua. Dark blue circles are the case of PopIII embedded in pristine gas. Light blue squares and cyan triangles show the case of PopIII photoionising slightly enriched gas, as indicated in the legend. In the case of PopIII, Nakajima & Maiolino (2022) use a Salpeter IMF with three different stellar ranges: 1–100  $M_{\odot}$ , 1–500  $M_{\odot}$ , and 50–500  $M_{\odot}$ ; these are coded with PopIII symbols of different sizes, as indicated in the legend. We note that, despite the high mass range explored in Nakajima & Maiolino (2022), a Salpeter IMF may not be appropriate for PopIII (e.g. de Bennassuti et al. 2014, 2017; Stacy et al. 2016;

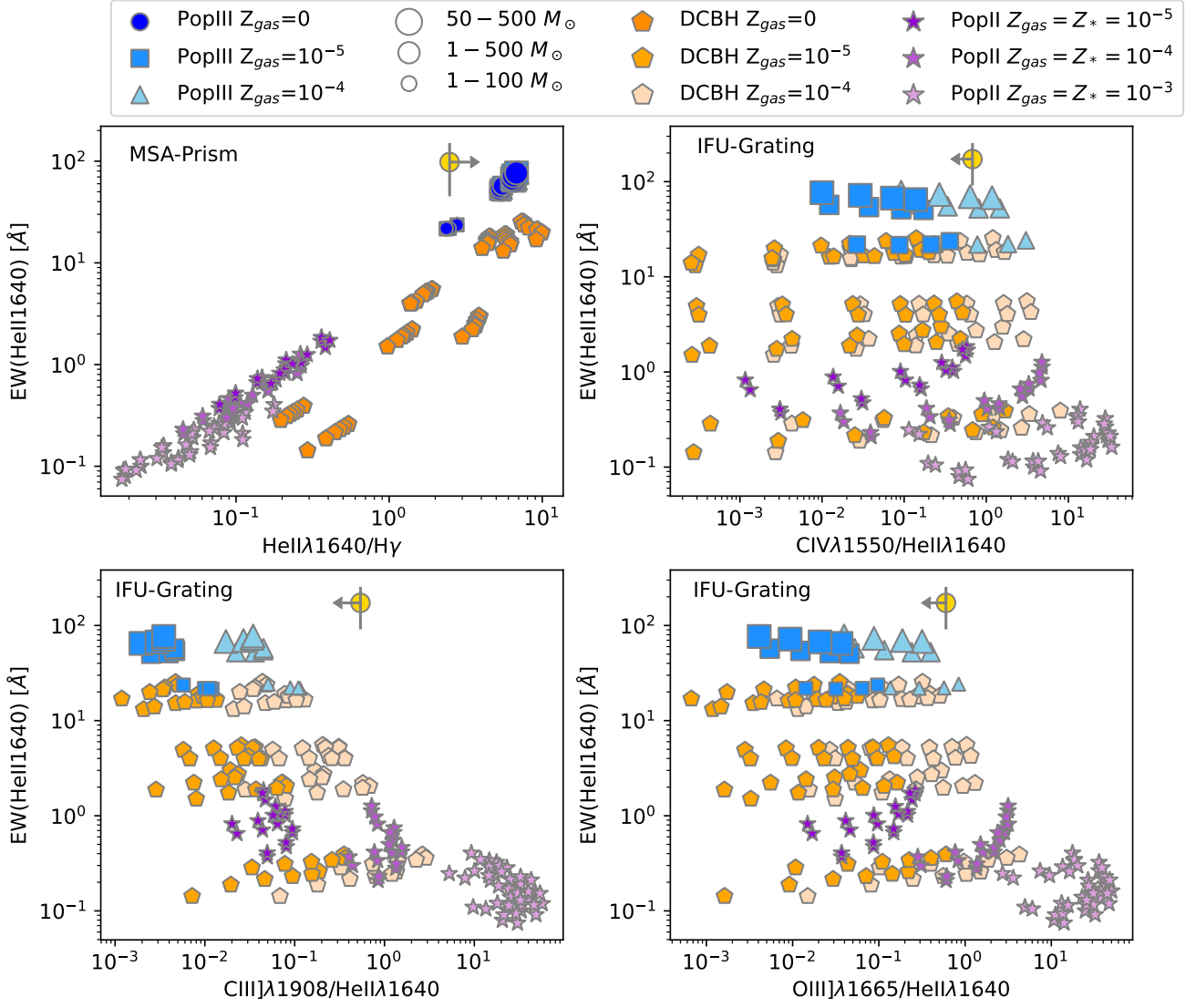


Fig. 6: Diagnostic diagrams showing the equivalent width of HeII $\lambda$ 1640 versus various line ratios: HeII/H $\gamma$ , CIV $\lambda$ 1550/HeII, CIII] $\lambda$ 1909/HeII, OIII] $\lambda$ 1665/HeII. Purple stars show PopII models with different (absolute) metallicities (color coded with different purple shadings), and where the gas and stars are assumed to have the same metallicity. Blue circles are models of PopIII stars in a pristine gas; light blue squares are models of PopIII stars in a mildly enriched gas, specifically  $Z_{\text{gas}} = 10^{-5}$ ; light blue triangles are models of PopIII stars in a more enriched gas, specifically  $Z_{\text{gas}} = 10^{-4}$ . The PopIII markers have different sizes depending on the stellar mass range assumed for the IMF, as indicated in the legend. Orange pentagons show the predictions for accreting Direct Collapse Black Holes embedded in gas with different (absolute) metallicities. The observational constraints on the HeII clump in the halo of GN-z11 are shown with a golden circle.

Venditti et al. 2023), and the EW(HeII) for PopIII may therefore have values even higher than those obtained by those models.

The constraints on the HeII clump in the halo of GN-z11 are shown with a golden circle. The continuum for estimating the EW(HeII) is extracted by extracting and interpolating the NIR-Cam photometries in the F150W, F200W and F277W bands (Table 3). Very little flux is observed in the aperture used to extract the HeII clump emission, and it is not even clear if such weak emission is associated with the HeII clump or with some emission from the foreground galaxy to the NE of the clump, or to the ‘haze’. Therefore, the inferred EW is more likely a lower limit. For the HeII/H $\gamma$  ratio we use the data from the prism, as H $\gamma$  is not covered by the new IFU observations (note that the HeII/H $\gamma$  is a lower limit given that H $\gamma$  is not detected, see Table 2; in this case we measure the EW separately by extracting the pho-

tometry at the corresponding aperture along the MSA shutter, as reported in Table 1. The resulting equivalent widths are given in Table 2. The EW(HeII) inferred for the clump and for the MSA spectrum are consistent with each other given the uncertainties. As said, these EW are likely lower limits.

Fig. 6 illustrates that the high EW(HeII $\lambda$ 1640) =  $172 \pm 76$  Å observed in the HeII clump is inconsistent, by orders of magnitude, with the PopII models, while consistent with the PopIII models. Furthermore, it requires a very top-heavy IMF, with an upper mass cutoff of at least  $500 M_{\odot}$ . Possibly an even higher stellar mass cutoff is needed, or, in addition to the high mass cutoff, an IMF more top-heavy than Salpeter, or perhaps a log-flat IMF (Chon et al. 2021), are required to explain the very large EW(HeII).

The lower limit on the HeII/H $\gamma$  ratio (Fig. 6 top left; see also Table 2) is nicely consistent with the constraint from the EW(HeII), i.e. requiring photoionisation from PopIII stars, and possibly with a top-heavy IMF. In contrast, the upper limits from the metal lines (see Table 2) are not very constraining in terms of metallicity and we cannot exclude that the PopIII stars are embedded in some moderately enriched gas, although the CIV/HeII upper limit is at the borderline with the models of PopIII living in a gas with metallicity of  $10^{-4}$ .

By using the PopIII models with the two top-heavy IMFs ( $1-500 M_{\odot}$  and  $50-500 M_{\odot}$ ) we infer the ratio between HeII luminosity and total, bolometric luminosity ( $10^{-2}$ ). This gives a bolometric luminosity of  $7.7 \times 10^{43}$  erg s $^{-1}$  for the PopIII in the clump. Assuming an Eddington limited luminosity, this gives a mass of only  $6 \times 10^5 M_{\odot}$ . Using the same IMF one can estimate the total stellar mass formed in the burst and associated with the observed luminosity (Schaerer 2003). Specifically, the inferred bolometric luminosity would give a total stellar mass of  $7 \times 10^5 M_{\odot}$ , similar to the value obtained above assuming an Eddington limited luminosity. These values for the total PopIII stellar mass are not far from the PopIII stellar mass expected by recent simulations. Indeed, these expect a halo hosting a PopII stellar mass similar to GN-z11 ( $\sim 8 \times 10^8 M_{\odot}$  in the extended component, Tacchella et al. 2023), to harbour a fractional mass of PopIII stars of about  $3 \times 10^{-4} - 1 \times 10^{-3}$ , i.e. a total PopIII stellar mass of  $\sim 2 - 8 \times 10^5 M_{\odot}$  (Yajima et al. 2022; Venditti et al. 2023; A. Venditti, priv. comm.).

It is worth noting that, in addition to the extended HeII emission, although the map is noisy, the HeII clump itself seems resolved and possibly extended over  $\sim 0.3''$ , i.e.  $\sim 1$  kpc. This is much larger than the expected size of a single PopIII sub-halo and it is much more likely that the extension is associated with a cluster of PopIII sub-halos. Indeed, according to recent simulations, PopIII sub-halos are expected to cluster in regions of a few kpc (Tornatore et al. 2007b; Venditti et al. 2023). Alternatively, the extension may trace a large clump of pristine gas which is being photoionised by a single halo of PopIII stars embedded in it.

We finally also consider the possibility that the HeII clump is ionized in-situ by an accreting Direct Collapse Black Hole (DCBH) seed in a pristine, or very low metallicity gas cloud. Nakajima & Maiolino (2022) have explored this case in their photoionization calculations, and these models are shown with orange pentagon symbols in Fig. 6. The darker orange symbols show the case of DCBH photoionizing pristine (zero metallicity) gas, while lighter shades of orange indicate the case of moderately enriched gas, as indicated in the legend. As for the PopII and PopIII case, models explore a broad range of densities and ionization parameters. Additionally, models explore a broad range of plausible ionizing shapes for the accreting DCBH (we defer to Nakajima & Maiolino 2022, for a more detailed description of the models). The DCBH models reach HeII equivalent widths much larger than PopII stars, however not as high as the PopIII with the most top-heavy IMF. In particular, the DCBH models do not reach the EW(HeII) required to explain the observation of the HeII clump. However, the difference is not huge (a factor of  $\sim 3-5$  within the errorbars), and we do not exclude that more extreme DCBH models could be consistent with the observations. Therefore, although the DCBH scenario is not favoured, it remains a possible alternative interpretation.

## 5. Conclusions

We have presented new NIRSpec-IFU observations of GN-z11, a remarkably luminous galaxy at  $z=10.6$ . We have also presented a re-analysis of the 2D MSA spectra of GN-z11 from the JADES survey. Unfortunately, a telescope guiding problem during the IFU observations resulted in GN-z11 being offset to the western edge of the FoV in various dither positions, so the focus of the paper has been on the analysis of the extension in the eastern part, while the properties of the western extension were only briefly analysed (a more detailed analysis of the western extension is deferred to after the repeated observations of the affected dithers, within the context of the same observing programme).

The main observational findings are the following:

- We detect a spectral feature at  $1.902 \mu\text{m}$  in a clump at  $\sim 0.5 - 0.6''$  ( $\sim 2$  kpc) to the NE of GN-z11. This wavelength corresponds to HeII $\lambda 1640$  at  $z=10.600$ , fully consistent with the redshift of GN-z11. The line is detected both in the MSA-prism ( $3.7\sigma$ ) and in the IFU-grating ( $5.5\sigma$ ).
- The HeII emission is also detected over a more extended area in the NE quadrant of GN-z11, possibly with a second (fainter) clump. There is also a HeII plume extending towards the West of GN-z11.
- Ly $\alpha$  and CIII] are also clearly extended and well resolved. Ly $\alpha$  has a sharp feature extending towards the SW of GN-z11, where bright CIII] also extends in a funnel-shaped geometry (however, we remind that these extended features towards the West will need to be re-examined with new data). At lower surface brightness Ly $\alpha$  also extends over a larger region of up to  $\sim 2$  kpc to the NE of GN-z11, and with a peak at about  $1.5$  kpc from the galaxy.

We investigate in detail these features, mostly focusing on the HeII emission, and reach the following conclusions:

- While HeII emission close to GN-z11 may be associated with photoionization by the AGN, simple photon budget arguments exclude that this is the case for the HeII clump, leaving *in-situ* ionisation as the only possibility.
- We show that the very high EW(HeII $\lambda 1640$ ) =  $172 \pm 76 \text{ \AA}$  cannot be explained in terms of photoionization by PopII (metal-poor) stars, while it is consistent with photoionization by PopIII stars.
- The very high EW(HeII) suggests that the putative PopIII stars must have a top-heavy IMF reaching an upper mass cutoff of at least  $500 M_{\odot}$ . The non-detection of H $\gamma$  (hence the lower limit on HeII/H $\gamma$ ) also supports this scenario.
- We infer that the mass of PopIII stars formed in the burst is about  $\sim 6 \times 10^5 M_{\odot}$ , which is not far from the fraction of PopIII stars in massive halos at these redshifts expected by some simulations.
- We also consider the alternative possibility of photoionization by a Direct Collapse Black Hole in the HeII clump. This scenario is less favoured, as it predicts a lower EW, but not by a large factor. Hence this scenario remains a possible interpretation, although less favoured.
- Finally, we suggest that the funnel-shaped CIII] extension, accompanied by the Ly $\alpha$  elongated feature towards the SW, traces the ionization cone of the AGN hosted in GN-z11.

*Acknowledgements.* We thank Alessandra Venditti, Harley Katz, Raffaella Schneider, Richard Ellis, and Stefania Salvadori for valuable comments. AJB acknowledges funding from the ‘‘FirstGalaxies’’ Advanced Grant from the European Research Council (ERC) under the European Union’s Horizon 2020 research and innovation programme (Grant agreement No. 789056). BER, BJ,

Table 1: Extraction apertures (given the IFU observation guiding problem, the IFU mask coordinates apply only once the cubes are registered to have the GN-z11 continuum matching the absolute coordinates given in Tacchella et al. (2023))

	RA	DEC	size('')	PA
HeII clump	12:36:25.514	+62:14:31.80	0.24×0.24	0
HeII large ap.	12:36:25.514	+62:14:31.62	0.48×0.60	0
MSA offset ap.	12:36:25.471	+62:14:31.78	0.20×0.20	19.9

Table 2: Measured fluxes, equivalent widths and upper limits in the apertures considered in this paper

Emission line	Flux $10^{-19}$ erg s $^{-1}$ cm $^{-2}$	EW Å
HeII clump small aperture		
HeII $\lambda$ 1640	5.0±0.94	172±76
CIV1550	<3.4	
OIII]1665	<2.7	
CIII]1909	<3.0	
HeII large aperture		
HeII $\lambda$ 1640	14.1±2.3	63±33
CIV1550	<8.7	
OIII]1665	<6.9	
CIII]1909	<7.7	
MSA offset aperture		
HeII $\lambda$ 1640	3.4±0.9	98±52
Hy	<1.37	

Table 3: Continuum fluxes in HeII clump from NIRCcam

Filter	Flux [nJy]
HeII clump small aperture	
F150W	4.4±1.8
F200W	2.2±1.6
F277W	3.1±0.9
HeII large aperture	
F150W	19.7±6.2
F200W	25.9±8.1
F277W	25.9±8.1
MSA offset aperture	
F150W	2.2±1.8
F200W	3.6±1.6
F277W	4.9±0.9

CNAW, DJE, EE, FS acknowledge support from the NIRCcam Science Team contract to the University of Arizona, NAS5-02015. DJE is also supported as a Simons Investigator. The research of CCW is supported by NOIRLab, which is managed by the Association of Universities for Research in Astronomy (AURA) under a cooperative agreement with the National Science Foundation. CW thanks the Science and Technology Facilities Council (STFC) for a PhD studentship, funded by UKRI grant 2602262. ECL acknowledges support of an STFC Webb Fellowship (ST/W001438/1). FDE, JS, RM, TL, WB acknowledge support by the Science and Technology Facilities Council (STFC), ERC Advanced Grant 695671 “QUENCH”. RM also acknowledges funding from a research professorship from the Royal Society. GC acknowledges the support of the INAF Large Grant 2022 “The metal circle: a new sharp view of the baryon cycle up to Cosmic Dawn with the latest generation IFU facilities”. GV, SCa acknowledge support by European Union’s HE ERC Starting Grant No. 101040227 - WINGS. HÜ gratefully acknowledges support by the Isaac Newton Trust and by the Kavli Foundation through a Newton-Kavli Junior Fellowship. JW acknowledges support from the ERC Advanced Grant 695671, “QUENCH”, and the Fondation MERAC. NL acknowledges support from the Kavli foundation. PRdP, MP, SA acknowledge support from Grant PID2021-127718NB-I00 funded by the Spanish Ministry of Science and Innovation/State Agency of Research (MICIN/AEI/10.13039/501100011033). MP also acknowledges support from the Programa Atracción de Talento de la Comunidad de Madrid via grant 2018-T2/TIC-11715. RS acknowledges support from a STFC Ernest Rutherford Fellowship (ST/S004831/1).

## References

- Abel, T., Bryan, G. L., & Norman, M. L. 2002, *Science*, 295, 93  
 Beers, T. C. & Christlieb, N. 2005, *ARA&A*, 43, 531  
 Böker, T., Arribas, S., Lützgendorf, N., et al. 2022, *A&A*, 661, A82  
 Böker, T., Beck, T. L., Birkmann, S. M., et al. 2023, *PASP*, 135, 038001  
 Bouwens, R. J., Illingworth, G. D., González, V., et al. 2010, *ApJ*, 725, 1587  
 Bowler, R. A. A., McLure, R. J., Dunlop, J. S., et al. 2017, *MNRAS*, 469, 448  
 Bromm, V., Coppi, P. S., & Larson, R. B. 1999, *ApJ*, 527, L5  
 Bromm, V. & Larson, R. B. 2004, *ARA&A*, 42, 79  
 Bromm, V., Yoshida, N., Hernquist, L., & McKee, C. F. 2009, *Nature*, 459, 49  
 Bunker, A. J., Saxena, A., Cameron, A. J., et al. 2023, *arXiv e-prints*, arXiv:2302.07256  
 Cassata, P., Le Fèvre, O., Charlot, S., et al. 2013, *A&A*, 556, A68  
 Chon, S., Omukai, K., & Schneider, R. 2021, *MNRAS*, 508, 4175  
 Clark, P. C., Glover, S. C. O., Klessen, R. S., & Bromm, V. 2011, *ApJ*, 727, 110  
 Cooke, R., Pettini, M., Steidel, C. C., Rudie, G. C., & Jorgenson, R. A. 2011, *MNRAS*, 412, 1047  
 de Bannassuti, M., Salvadori, S., Schneider, R., Valiante, R., & Omukai, K. 2017, *MNRAS*, 465, 926  
 de Bannassuti, M., Schneider, R., Valiante, R., & Salvadori, S. 2014, *MNRAS*, 445, 3039  
 Feltre, A., Charlot, S., & Gutkin, J. 2016, *MNRAS*, 456, 3354  
 Ferruti, P., Jakobsen, P., Giardino, G., et al. 2022, *A&A*, 661, A81  
 Fossati, M., Fumagalli, M., Lofthouse, E. K., et al. 2021, *MNRAS*, 503, 3044  
 Frebel, A., Johnson, J. L., & Bromm, V. 2007, *MNRAS*, 380, L40

- Greif, T. H., Bromm, V., Clark, P. C., et al. 2012, *MNRAS*, 424, 399
- Greif, T. H., Springel, V., White, S. D. M., et al. 2011, *ApJ*, 737, 75
- Guo, Y., Maiolino, R., Jiang, L., et al. 2020, *ApJ*, 898, 26
- Harikane, Y., Ouchi, M., Shibuya, T., et al. 2018, *ApJ*, 859, 84
- Hartwig, T., Bromm, V., Klessen, R. S., & Glover, S. C. O. 2015, *MNRAS*, 447, 3892
- Hartwig, T., Yoshida, N., Magg, M., et al. 2018, *MNRAS*, 478, 1795
- Hirano, S., Hosokawa, T., Yoshida, N., et al. 2014, *ApJ*, 781, 60
- Jaacks, J., Finkelstein, S. L., & Bromm, V. 2019, *MNRAS*, 488, 2202
- Jaacks, J., Thompson, R., Finkelstein, S. L., & Bromm, V. 2018, *MNRAS*, 475, 4396
- Jakobsen, P., Ferruit, P., Alves de Oliveira, C., et al. 2022, *A&A*, 661, A80
- Jeon, M., Bromm, V., Pawlik, A. H., & Milosavljević, M. 2015, *MNRAS*, 452, 1152
- Johnson, J. L. 2010, *MNRAS*, 404, 1425
- Kashlinsky, A. & Rees, M. J. 1983, *MNRAS*, 205, 955
- Katz, H., Kimm, T., Ellis, R. S., Devriendt, J., & Slyz, A. 2022, arXiv e-prints, arXiv:2207.04751
- Klessen, R. S. & Glover, S. C. O. 2023, arXiv e-prints, arXiv:2303.12500
- Liu, B. & Bromm, V. 2020, *MNRAS*, 497, 2839
- Maiolino, R., Scholtz, J., Witstok, J., et al. 2023, arXiv e-prints, arXiv:2305.12492
- Nakajima, K. & Maiolino, R. 2022, *MNRAS*, 513, 5134
- Oesch, P. A., Bouwens, R. J., Illingworth, G. D., Labbé, I., & Stefanon, M. 2018, *ApJ*, 855, 105
- Oesch, P. A., Brammer, G., van Dokkum, P. G., et al. 2016, *ApJ*, 819, 129
- Oh, S. P., Haiman, Z., & Rees, M. J. 2001, *ApJ*, 553, 73
- Pagnini, G., Salvadori, S., Rossi, M., et al. 2023, *MNRAS*, 521, 5699
- Pallottini, A., Ferrara, A., Gallerani, S., Salvadori, S., & D'Odorico, V. 2014, *MNRAS*, 440, 2498
- Perna, M., Arribas, S., Marshall, M., et al. 2023, arXiv e-prints, arXiv:2304.06756
- Planck Collaboration, Aghanim, N., Akrami, Y., et al. 2020, *A&A*, 641, A6
- Rauscher, B. J., Arendt, R. G., Fixsen, D. J., et al. 2012, in *Society of Photo-Optical Instrumentation Engineers (SPIE) Conference Series*, Vol. 8453, High Energy, Optical, and Infrared Detectors for Astronomy V, ed. A. D. Holland & J. W. Beletic, 84531F
- Rigby, J., Perrin, M., McElwain, M., et al. 2023, *PASP*, 135, 048001
- Rossi, M., Salvadori, S., & Skúladóttir, Á. 2021, *MNRAS*, 503, 6026
- Saccardi, A., Salvadori, S., D'Odorico, V., et al. 2023, *ApJ*, 948, 35
- Salvadori, S., D'Odorico, V., Saccardi, A., Skuladottir, A., & Vanni, I. 2023, arXiv e-prints, arXiv:2305.07706
- Sarmento, R., Scannapieco, E., & Cohen, S. 2018, *ApJ*, 854, 75
- Schaerer, D. 2003, *A&A*, 397, 527
- Sobral, D., Matthee, J., Darvish, B., et al. 2015, *ApJ*, 808, 139
- Stacy, A., Bromm, V., & Lee, A. T. 2016, *MNRAS*, 462, 1307
- Susa, H., Hasegawa, K., & Tominaga, N. 2014, *ApJ*, 792, 32
- Tacchella, S., Eisenstein, D. J., Hainline, K., et al. 2023, arXiv e-prints, arXiv:2302.07234
- Tan, J. C. & McKee, C. F. 2004, *ApJ*, 603, 383
- Tegmark, M., Silk, J., Rees, M. J., et al. 1997, *ApJ*, 474, 1
- Tornatore, L., Ferrara, A., & Schneider, R. 2007a, *MNRAS*, 382, 945
- Tornatore, L., Ferrara, A., & Schneider, R. 2007b, *MNRAS*, 382, 945
- Trinca, A., Schneider, R., Maiolino, R., et al. 2023a, *MNRAS*, 519, 4753
- Trinca, A., Schneider, R., Valiante, R., et al. 2023b, arXiv e-prints, arXiv:2305.04944
- Tumlinson, J., Giroux, M. L., & Shull, J. M. 2001, *ApJ*, 550, L1
- Tumlinson, J. & Shull, J. M. 2000, *ApJ*, 528, L65
- van Dokkum, P. G. 2001, *PASP*, 113, 1420
- Vanzella, E., Loiacono, F., Bergamini, P., et al. 2023, arXiv e-prints, arXiv:2305.14413
- Venditti, A., Graziani, L., Schneider, R., et al. 2023, *MNRAS*, 522, 3809
- Ventura, E. M., Trinca, A., Schneider, R., et al. 2023, *MNRAS*, 520, 3609
- Vikaus, A., Zackrisson, E., Schaefer, D., et al. 2022, *MNRAS*, 512, 3030
- Volonteri, M., Habouzit, M., & Colpi, M. 2023, *MNRAS*, 521, 241
- Yajima, H., Abe, M., Fukushima, H., et al. 2022, arXiv e-prints, arXiv:2211.12970
- Zackrisson, E., Rydberg, C.-E., Schaefer, D., Östlin, G., & Tuli, M. 2011, *ApJ*, 740, 13
- <sup>3</sup> Department of Physics and Astronomy, University College London, Gower Street, London WC1E 6BT, UK
- <sup>4</sup> Centro de Astrobiología (CAB), CSIC-INTA, Cra. de Ajalvir Km. 4, 28850- Torrejón de Ardoz, Madrid, Spain
- <sup>5</sup> Institute of Astronomy, University of Cambridge, Madingley Road, Cambridge CB3 0HA, UK
- <sup>6</sup> Scuola Normale Superiore, Piazza dei Cavalieri 7, I-56126 Pisa, Italy
- <sup>7</sup> National Astronomical Observatory of Japan, 2-21-1 Osawa, Mitaka, Tokyo 181-8588, Japan
- <sup>8</sup> Center for Astrophysics - Harvard & Smithsonian, 60 Garden St., Cambridge MA 02138 USA
- <sup>9</sup> Department of Physics, University of Oxford, Denys Wilkinson Building, Keble Road, Oxford OX1 3RH, UK
- <sup>10</sup> Sorbonne Université, CNRS, UMR 7095, Institut d'Astrophysique de Paris, 98 bis bd Arago, 75014 Paris, France
- <sup>11</sup> INAF - Osservatorio Astrofisico di Arcetri, largo E. Fermi 5, 50127 Firenze, Italy
- <sup>12</sup> European Southern Observatory, Karl-Schwarzschild-Strasse 2, 85748 Garching, Germany
- <sup>13</sup> Centre for Astrophysics Research, Department of Physics, Astronomy and Mathematics, University of Hertfordshire, Hatfield AL10 9AB, UK
- <sup>14</sup> Max-Planck-Institut für Astronomie, Königstuhl 17, D-69117, Heidelberg, Germany
- <sup>15</sup> Steward Observatory University of Arizona 933 N. Cherry Avenue Tucson AZ 85721, USA
- <sup>16</sup> AURA for European Space Agency, Space Telescope Science Institute, 3700 San Martin Drive. Baltimore, MD, 21210
- <sup>17</sup> Department of Astronomy, University of Wisconsin-Madison, 475 N. Charter St., Madison, WI 53706 USA
- <sup>18</sup> Department of Astronomy and Astrophysics, University of California, Santa Cruz, 1156 High Street, Santa Cruz, CA 95064, USA
- <sup>19</sup> Astrophysics Research Institute, Liverpool John Moores University, 146 Brownlow Hill, Liverpool L3 5RF, UK
- <sup>20</sup> NSF's National Optical-Infrared Astronomy Research Laboratory, 950 North Cherry Avenue, Tucson, AZ 85719, USA

<sup>1</sup> Kavli Institute for Cosmology, University of Cambridge, Madingley Road, Cambridge, CB3 0HA, UK

<sup>2</sup> Cavendish Laboratory, University of Cambridge, 19 JJ Thomson Avenue, Cambridge CB3 0HE, UK

## Appendix A: NIRSpect-ICU continuum map

Fig. A.1 shows the map of the continuum obtained by collapsing continuum channels near the CIII]1909 emission, with contours of the continuum-subtracted CIII] line map overlaid. The continuum map does not show any elongation, demonstrating that the CIII] elongation is not an artefact of the data processing.

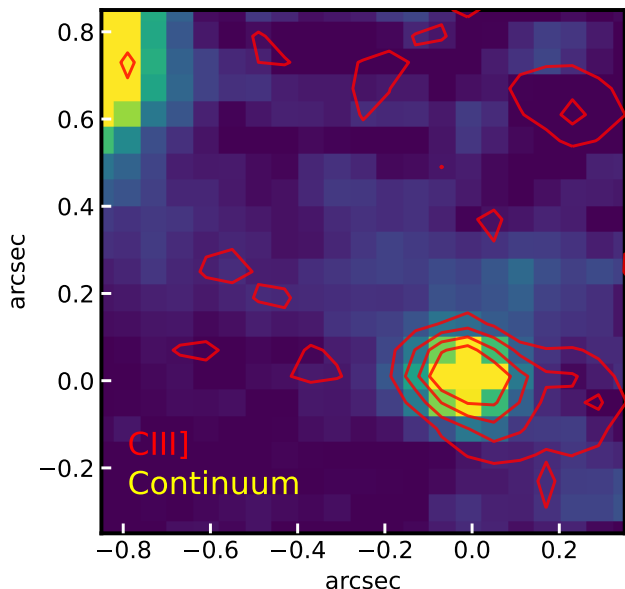


Fig. A.1: Map of the GN-z11 continuum around the CIII] emission line with the CIII] contours overlaid (red). Contours are 2, 4, 6 and 8  $\sigma$  levels. The CIII] emission shows an extension to the East while the continuum appears like a point source.

## Appendix B: Interlopers and other emission-line sources

We searched the region around GN-z11 for possible interlopers. There is a disc galaxy with bright H $\alpha$  emission 1.1 arcsec North-East of GN-z11. We integrate the flux of this galaxy (dark red contours in Fig. B.1, left) and show the resulting spectrum (top right panel); at the redshift of  $z = 2.028$ , there is no strong emission line that may contaminate the HeII emission (i.e., near  $\lambda = 1.90 \mu\text{m}$ ). Besides, at the location of the HeII ‘blob’ (blue contours), the strength of any emission line due to the interloper would be even weaker than what shown in the extracted spectrum. We can therefore exclude that the line we identify as HeII is due to misidentified line emission at  $z = 2.028$ .

The red contours show the extraction box around the ‘haze’ (cf. Tacchella et al. 2023). The corresponding spectrum shows an emission line at  $\lambda = 2.331 \mu\text{m}$ . We tentatively identify this line as either [OIII] $\lambda 5007$  – typically the strongest emission line in low-mass galaxies. This would mean the ‘haze’ was a  $z = 3.665$  interloper – consistent with the photometric redshift of Tacchella et al. (2023). If the line was H $\alpha$ , we would expect to see [OIII] $\lambda 5007$  at bluer wavelength (low-mass galaxies have typically little dust), but no suitable emission is found. Either way, there is no strong emission line from this interloper near the wavelength of HeII.

Finally, we detect an emission line to the SW of GN-z11 (bottom panel of Fig. B.1). This source has no continuum and therefore no photometric redshift. We are thus unable to identify

its redshift. Clearly, however, no contamination can arise from this region over to the HeII blob.

## Appendix C: Spectrum extracted from large aperture excluding regions closer to GN-z11

The HeII emission in GN-z11 is so faint that it cannot contribute to the spectrum shown in the right panel of Fig. 4 extracted from the large aperture drawn with a yellow box in Fig. 1 (Tab. 1), or else many other much stronger lines from GN-z11 would be seen in the spectrum. However, in order to further exclude any contamination, we have re-extracted the spectrum from the same aperture by excluding the region closer than 0.3'' (i.e. 6 times the radius of the PSF at this wavelength) from GN-z11. The resulting spectrum is shown in Fig. C.1, which is essentially unchanged with respect to Fig. 4-right; if anything, the HeII detection is slightly more significant in this spectrum. Therefore, it is confirmed that the HeII flux from GN-z11 does not contribute to the flux observed in that aperture.

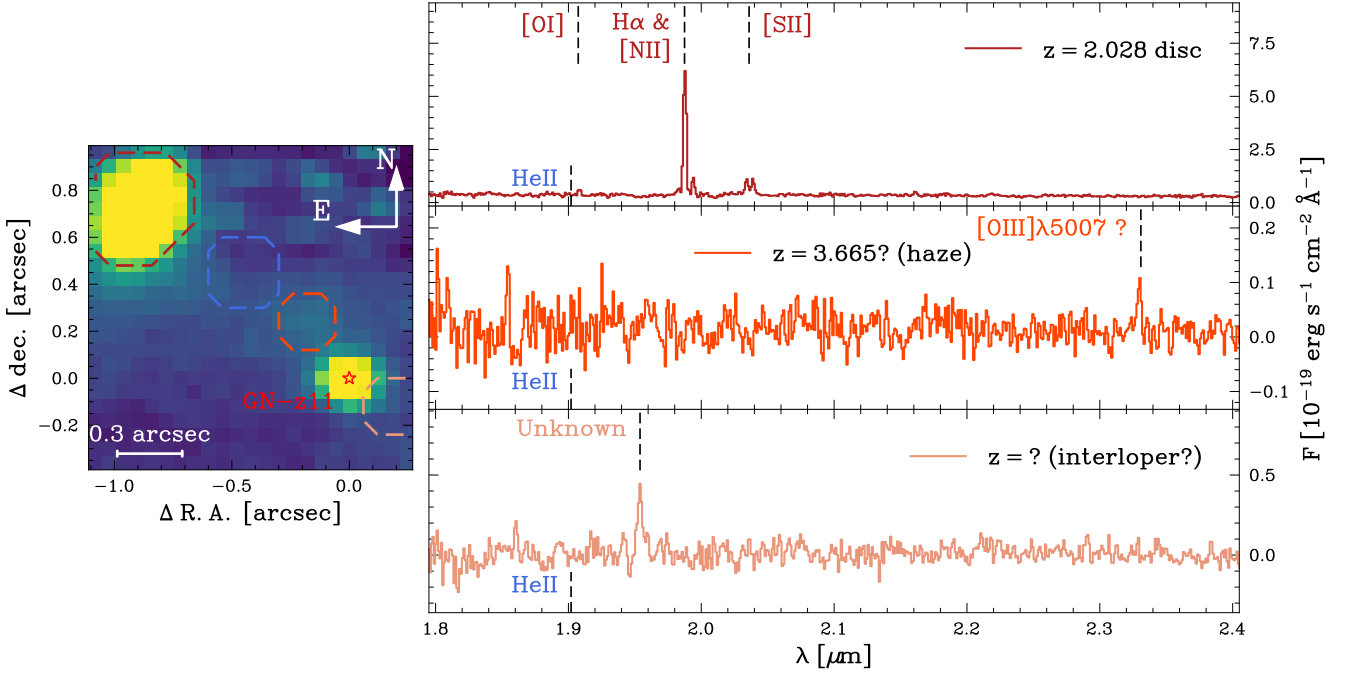


Fig. B.1: Map of the continuum in a region centred at the ‘haze’, highlighting a bright disc galaxy at  $z = 2$ , the haze itself, and a region South-West of GN-z11. The spectra of these three sources/regions are shown in the right panels, highlighting the location of our HeII detection, as well as other detected emission lines. The galaxy at  $z = 2$  does not have any bright feature at wavelengths close to  $1.902 \mu m$ . The haze presents a single emission line which we tentatively identify as [OIII] $\lambda$ 5007 at  $z = 3.66$  – which would be consistent with the photometric redshift from Tacchella et al. (2023). Finally, we detect an emission line in the SW lobe of GN-z11. At the redshift of GN-z11, this line would correspond to a rest-frame wavelength of  $0.1684 \mu m$  – which we do not trace to any notable emission line.

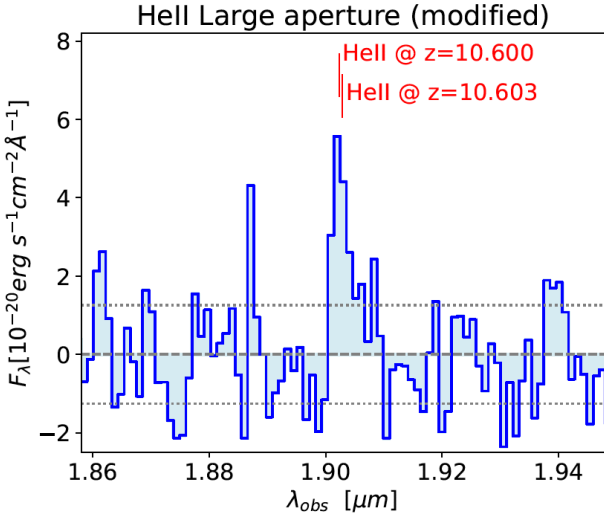


Fig. C.1: Spectrum extracted from the same extracted aperture at the spectrum in the right panel of Fig. 4, i.e. the aperture marked in yellow in Fig. 1 (Tab. 1), but where the regions closer than  $0.3''$  to GN-z11 were excluded. The spectrum is essentially unchanged with respect to the spectrum extracted from the entire aperture.